

Room-temperature ladder-type optical memory compatible with single photons from InGaAs quantum dots

Benjamin Maass,^{1,2,*} Norman Vincenz Ewald,^{1,3} Avijit Barua,³ Stephan Reitzenstein,³ and Janik Wolters^{1,2}

¹*German Aerospace Center (DLR), Institute of Optical Sensor Systems, Rutherfordstraße 2, 12489 Berlin, Germany.*

²*Institute of Optics and Atomic Physics (IOAP),*

Technische Universität Berlin, Hardenbergstraße 36, 10623 Berlin, Germany.

³*Institute of Solid State Physics (IFKP), Technische Universität Berlin, Hardenbergstraße 36, 10623 Berlin, Germany.*

(Dated: February 23, 2024)

On-demand storage and retrieval of quantum information in coherent light-matter interfaces is a key requirement for future quantum networking and quantum communication applications. Alkali vapor memories offer scalable and robust high-bandwidth storage at high repetition rates which makes them a natural fit to interface with solid-state single-photon sources. Here, we experimentally realize a room-temperature ladder-type atomic vapor memory that operates on the Cs D1 line. We provide a detailed experimental characterization and demonstration of on-demand storage and retrieval of weak coherent laser pulses with 0.06 photons per pulse at a high signal-to-noise ratio of SNR = 830(80). The memory achieves a maximum internal storage efficiency of $\eta_{\text{int}} = 15(1)\%$ and an estimated 1/e-storage time of $\tau_s \approx 32$ ns. Benchmark properties for the storage of single photons from inhomogeneously broadened state-of-the-art solid-state emitters are estimated from the performance of the memory. Together with the immediate availability of high-quality InGaAs quantum dots emitting at 895 nm, these results provide clear prospects for the development of a heterogeneous on-demand quantum light interface.

I. INTRODUCTION

Quantum communication with single photons as flying qubits requires both quantum light sources and control over the timing and synchronization of photons. The ability of optical quantum memories to store and retrieve photons on demand [1–3] allows for synchronization of probabilistic photons [4], buffering and entanglement swapping in quantum repeater networks [5–8]. A coherent light-matter interface is thus an integral part of future photonic quantum communication networks [2, 9]. Technological applications will benefit from high bandwidths on the order of GHz and large photon rates, while maintaining low noise and high end-to-end memory efficiencies [1–3, 9]. A prominent host matter for an optical quantum memory is room-temperature alkali vapor contained in an evacuated glass cell [1–3]. Large-scale field applications, and air- and spaceborne operations of such memory devices are under investigation [10, 11], enabled by the platform’s technological simplicity when compared to laser-cooled or cryogenic platforms. In room-temperature alkali vapors, coherent optical control over the light-matter interaction has been implemented in various atomic three-level systems, notably in Λ -type and ladder-type (Ξ) configurations. Coupling schemes such as electromagnetically-induced transparency (EIT) [12], off-resonant Raman transitions [13], and Autler-Townes-splitting [14] and atomic frequency comb protocols [15] are employed.

In ladder-type level configurations, GHz-bandwidth heralded single photons have been stored by two-photon

off-resonant cascaded absorption (ORCA) on the D2 line of Cs [16]. Moreover, a fast ladder memory (FLAME) on the D2 line of Rb enabled synchronisation of single photons stemming from identical, and thus intrinsically well-matched, atomic vapors [17], resulting in an enhanced photon pair coincidence rate [4]. In ^{87}Rb vapor, the ORCA protocol on the D2 line has enabled Doppler-limited storage times of 1.10(2) ns [18]. In Λ -type Rb vapor, a bandwidth of 660 MHz has been achieved, suitable for single photons from semiconductor quantum dots [19]. Storage and retrieval of single photons from an SPDC source in a Λ -type memory has been demonstrated [20].

Quantum dots can emit deterministically, with high brightness and low multi-photon contribution [21], and are excellent building blocks for photonic quantum information technology [22, 23]. Thus, several attempts have been made to coherently interface single photons from semiconductor quantum dots with alkali vapor quantum memories. Atomic vapor was used as spectrally selective and tunable delay line for quantum dot photons [24–26]. Also, quantum dot photons were delayed by 5 ns due to strong dispersion between two hyperfine-split excited state transitions of the Cs D1 line, and the distortion of their wavepacket was analyzed [27]. More recently, a coherent exchange of quanta between single photons from a GaAs quantum dot and an atomic ensemble in a ^{87}Rb vapor has been shown [28]. Furthermore, photons from quantum dots embedded in semiconductor nanowires have been slowed down in an atomic vapor [29]. Lastly, photons with a 800 ps-long exponential envelope from an InAs quantum dot source in the telecom range have been stored for 800 ps in ^{87}Rb vapor in a ladder-type configuration [30].

* benjamin.maass@dlr.de

Here, we employ a ladder-type memory on the Cs D1 line, allowing for low-noise storage and retrieval of high-bandwidth photons in the favorable NIR wavelength region compatible with InGaAs quantum dot-based single-photon sources. The memory is characterized in terms of its $1/e$ -storage time τ_s , and its internal and end-to-end efficiencies, denoted η_{int} and η_{e2e} , respectively. We measure the noise floor and the spectral acceptance window $\mathcal{A}\mathcal{W}$ to estimate the influence of external photon sources with varying photon energy. The laser setup offers the ability to adapt the control pulses in laser frequency, power, pulse length, pulse number per storage trial, and timing intervals.

II. MEMORY PROTOCOL

We operate the memory device with signal photons on the D1 line of Cs, as depicted in Fig. 1a. A strong control field at a wavelength of 876 nm couples the intermediate $6P_{1/2}$ level to the $6D_{3/2}$ level and creates an EIT-window for the signal photons. Pulsed operation coherently maps the signal field onto a collective orbital coherence of the cesium atoms between the ground state and the storage state $6D_{3/2}$, the spinwave. Time-reversed operation, i.e. for symmetric pulses re-applying the control pulse, retrieves the initial signal photon. In this memory scheme, the main source of decoherence of the shared excitation is motional dephasing. The wavevector mismatch of the signal and control fields determines the wavelength of the spinwave, here $43.5\ \mu\text{m}$, and therewith the time scale of the spinwave decay. This relation is depicted in Fig. 3 and further discussed in Sec. IV A. In ladder-type memories the storage state is effectively unpopulated in thermal equilibrium, and the frequency mismatch between the signal and control transitions is very large compared to the Doppler-broadened linewidths. These two facts lead to extremely high signal-to-noise ratios (SNR). The storage time of the two-photon ladder-type memory is ultimately limited by the lifetime of the employed upper state. It has been shown that the limitations of motional dephasing can be overcome by dynamical decoupling of the storage level with an additional optical dressing field [4].

III. EXPERIMENTAL SETUP

The setup as depicted in Fig. 1b consists of the signal generation, the control generation and the memory unit. We describe the individual parts and their synchronization in the next sections.

A. Cs Cell and Heating System

The cylindrical vapor cell is 25 mm in diameter and 25 mm in length. The requirement for a homogeneous

optical field in the interaction area limits the Rayleigh range to the length of the cell and thereby the beam waists of signal and control lasers as well. In this experiment we chose a signal beam diameter of $100\ \mu\text{m}$ and a control beam diameter of $145\ \mu\text{m}$ at the center of the glass cell. Since the memory protocol is faster than the time scale of decoherence due to cesium-cesium collisions the experiment does not require a buffer-gas filled cell. A customized heating system made of a spring-loaded copper block with a heater allows for uniform heating of the glass cell to a temperature of up to 120°C while preventing condensation on the entrance windows.

B. Lasers, Pulse Generation and Timing Controls

The signal beam is generated by a continuous wave (CW) 894 nm distributed-feedback laser diode (DFB). A fraction of the beam is used for Doppler-free spectroscopy, which serves, in addition to a wavemeter with 100 MHz resolution, as a wavelength reference. An electro-optical amplitude modulator (EOM) generates signal pulses with a rise time of 500 ps. After attenuation to single-photon level with neutral-density (ND) filters, the signal beam is directed into the memory cell. The control beam is generated by a CW 876 nm external-cavity diode laser (ECDL) with an output power of up to 50 mW. The control pulses are carved from the CW laser with an EOM and subsequently amplified in a tapered amplifier (TA). The high-power output of the TA is then frequency-filtered with a 10 nm bandpass filter and a 1 nm narrow-band filter to remove the amplified spontaneous emission (ASE) background emerging from the TA. Pulse shaping with the EOMs allows for 1 ns-long (FWHM) pulses. The electronic control signals for the EOMs are generated with a 512 bit programmable pulse generator (PPG) with a repetition rate of 10 MHz and a resolution of 200 ps. The pulses are synchronized using a digital delay generator with 10 ps resolution. The shape of the pulses and the extinction of the EOMs are monitored on additional photodiodes. The setup allows for variable adjustment of pulse lengths and timings of both the signal and control lasers independently. The repetition rate of the experiment can easily be matched to external single-photon sources.

C. Signal Filtering and Detection

The counterpropagating and orthogonally polarized signal and control pulses overlap inside the cesium cell. The control pulses are separated in polarization and monitored on a fast photodiode. After being stored in the memory cell, the transmitted signal is also polarization-selected. After a series of broadband filters and a 1 nm narrow-band interference filter, the transmitted signal is coupled into a polarization-maintaining optical fiber that is connected to a superconducting nanowire single-

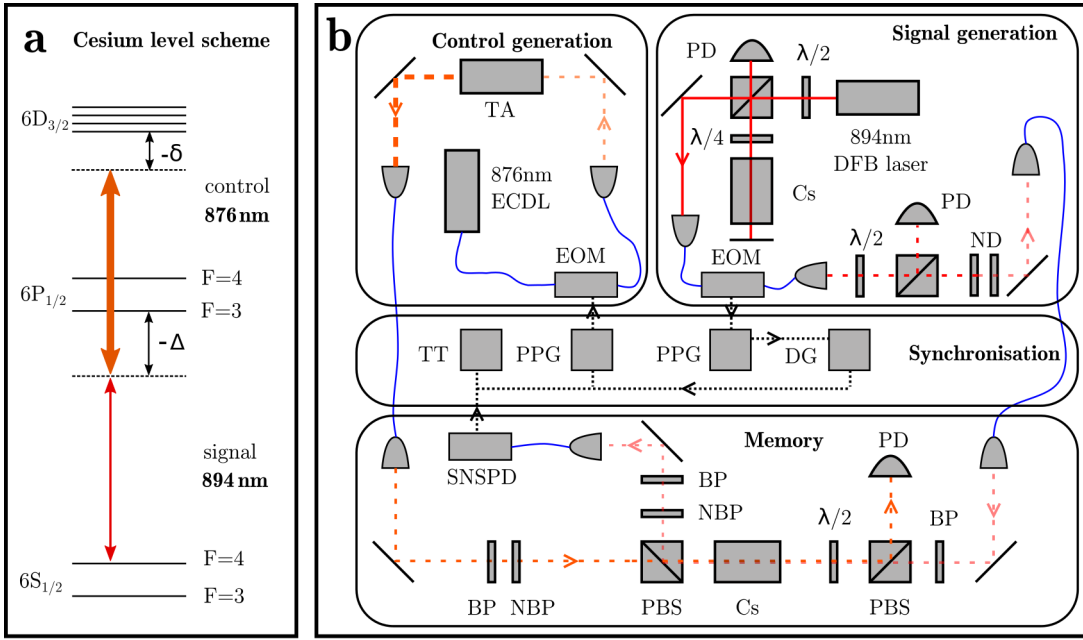


FIG. 1. Overview of the experiment. (a) Reduced level scheme of Cs. Signal and control laser in a ladder-type configuration with detuning Δ and two-photon detuning δ . (b) Experimental setup. Control pulses are generated with an electro-optical amplitude modulator (EOM) and subsequently amplified by a tapered amplifier (TA). Spectral filtering is achieved with a bandpass filter (BP) and a narrow-bandpass filter (NBP). A Doppler-free cesium (Cs) spectroscopy serves as a frequency reference for the signal laser. Signal pulses are generated with an EOM and monitored using a fast photodiode (PD). The signal beam is attenuated to single-photon level with neutral-density filters (ND). Counterpropagating signal and control pulses overlap inside the heated vapor cell (Cs). Signal photons are detected with a superconducting nanowire single-photon detector (SNSPD). Control leakage is suppressed by spatial, polarization and spectral filtering (BP, NBP). Programmable pulse generators (PPG) drive the EOMs and are synchronised with a digital delay generator (DG).

photon detector (SNSPD) with a nominal detection efficiency of 0.85 and a temporal resolution of 50 ps.

IV. CHARACTERIZATION AND RESULTS

In this section we characterize the memory and evaluate its performance regarding the retrieval time, the signal detuning and the optical depth. Additionally, we determine the spectral acceptance window of the memory and use the results to benchmark the memory performance for the feasibility of storing single photons from realistic quantum dot devices.

A. Optimization of Efficiency and Storage Time

Fig. 2 shows the histogrammed result of a typical storage and retrieval experiment. Leakage due to imperfect storage of incoming photons produces the read-in peak (shaded red). The photons in the read-out peak (shaded green) are retrieved from the atomic ensemble by the second control laser pulse after a delay of 17.4(1) ns. The shaded areas mark the integration windows for the efficiency analysis. The noise curve is taken with the input signal blocked, i.e. it contains both the

leaked control laser light and the integrated dark counts from the detector. The noise floor stems from insufficient suppression by the EOMs, electrical noise from the pulse generation and EOM bias drifts. A far-detuned (~ 6 GHz) signal measurement without the control laser serves as a reference for the signal input. We calculate the internal memory efficiency as the ratio of integrated counts within the retrieved signal peak and the reference measurement, $\eta_{\text{int}} = N_{\text{ret}}/N_{\text{in}}$, and find a maximum value of $\eta_{\text{int}} = 15(1)\%$ at 17.4(2) ns storage time. Including the setup transmission and the detection efficiency, we achieve an end-to-end memory efficiency of $\eta_{\text{e2e}} = 2.2(2)\%$. We expect an increased end-to-end efficiency by straightforward improvements of the setup transmission, e.g. using an anti-reflective coated Cs cell in future experiments. In a separate experiment with long integration time the low noise floor and an SNR of 830(80) is confirmed.

The measured dynamics of the internal storage efficiency are displayed in Fig. 3. We scan the storage time τ_s by adapting the timing of the retrieval control pulse. The memory is operated at 200 MHz red-detuning and the cell temperature is optimized, as discussed later and presented in Fig. 4. The peak Rabi frequency of the Gaussian control pulses is estimated to be $2\pi \cdot 900(30)$ MHz, given the measured CW laser power and the beam geom-

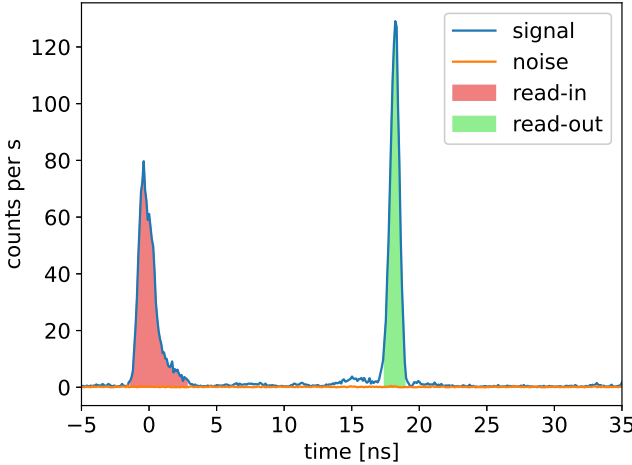


FIG. 2. Exemplary storage trace. Histogrammed (100 ps per time bin) storage and retrieval of 800 ps FWHM-long signal pulses attenuated to 0.06 photons per pulse at 200 MHz red-detuning from the $F = 4$ to $F' = 3$ transition of the D1 line. The control pulses have a FWHM of 1 ns and yield a peak Rabi frequency of $\Omega = 2\pi \cdot 900(30)$ MHz. At the retrieval time of $17.4(1)$ ns, the memory achieves an internal efficiency of $\eta_{\text{int}} = 15(1)\%$. The shaded areas mark the integration windows for the efficiency calculations.

etry as described in Sec. III. Retrieval times $\tau_s < 3$ ns are inaccessible because of otherwise temporally overlapping read-in and read-out control pulses. The data shows strong oscillatory spinwave dynamics that can be attributed to multiple addressed hyperfine states of the $6D_{3/2}$ storage level. This results in a beating of the generated spinwaves with the frequency splittings within the hyperfine manifold. It has been shown that this beating can be suppressed if only one hyperfine state is addressed by the signal field when circularly pumping into a stretched state [17]. The model introduced in Ref. [17] (solid line) qualitatively reproduces the data. The inhomogeneous dephasing time of the spinwave depends on its wavelength, determined by the wavevector mismatch of signal and control laser, and the thermal velocity of the atoms [31]. The inset of Fig. 3 depicts the relation between the theoretical dephasing times and the measured $1/e$ -storage times that have been reported in previously ladder-type memories (Thomas2023 [18], Kaczmarek2018 [16], and Finkelstein2018 [17]). For the level configuration in Fig. 1a, we expect a $1/e$ -storage time of about $\tau_s \approx 32$ ns, which is consistent with the data. The gray-dashed line and the shaded area estimate the exponential envelope of the spinwave oscillations from the red-highlighted maxima. The zero-time storage efficiency cannot be faithfully determined from the data. All following data is acquired at the maximum efficiency retrieval time of 17.4 ns. Future experiments will also shed light on additional inhomogeneous decay mechanisms such as spin-exchange collisions or atoms leaving the interaction area.

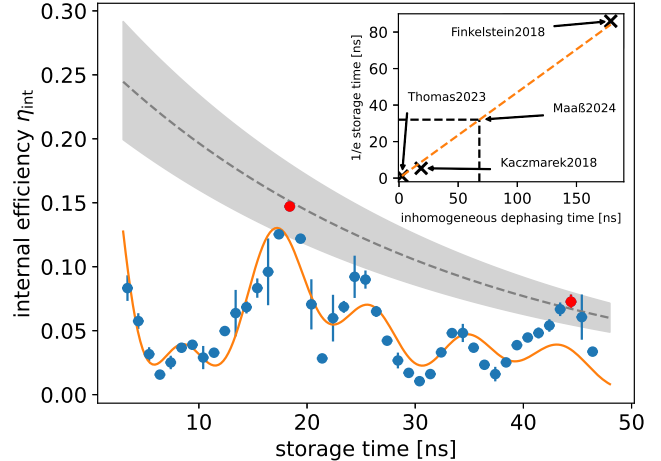


FIG. 3. Measured dynamics of the internal storage efficiency. In every step, the pulse timings are optimized. The peak Rabi frequency is estimated to $2\pi \cdot 900(30)$ MHz. Errors represent fit uncertainties and time resolution of the pulse generator. Integration times long compared to the inverse repetition rate render statistical errors negligible w.r.t. fit errors. The inset shows the relation between the inhomogeneous dephasing time and the $1/e$ -storage time as reported in the literature. The gray-shaded area estimates the exponential envelope of the spinwave oscillations.

The influence of the cell temperature on the internal memory efficiency is presented in Fig. 4. We find an optimum working point that shifts to higher temperatures for larger signal detunings Δ . The theory for optimal light storage [32] suggests that the memory efficiency increases monotonically with the optical depth (OD) of the atomic vapor. In contrast to this theory, and in agreement with other experiments [33, 34], we observe a decrease in efficiency if the OD is too high for a given detuning. Additional leakage channels, such as four-wave mixing and Raman scattering processes are suggested as possible sources for the observed decrease. However, this cannot hold as an explanation in this case because the two-color ladder-type configuration inhibits these types of mechanisms. Further research is necessary to gain a deeper understanding of the underlying mechanisms. Here, we have constrained the data evaluation to red-detuned signal input because the efficiencies are much lower in the blue-detuned regime. We attribute this behavior to additional spinwave dephasing due to increased coupling to the $F' = 4$ intermediate state under blue-detuning.

B. Spectral Acceptance Window

Solid-state single-photon sources such as self-assembled quantum dots usually suffer from an inhomogeneous broadening of the emission linewidth due to spectral diffusion [35]. It is thus important

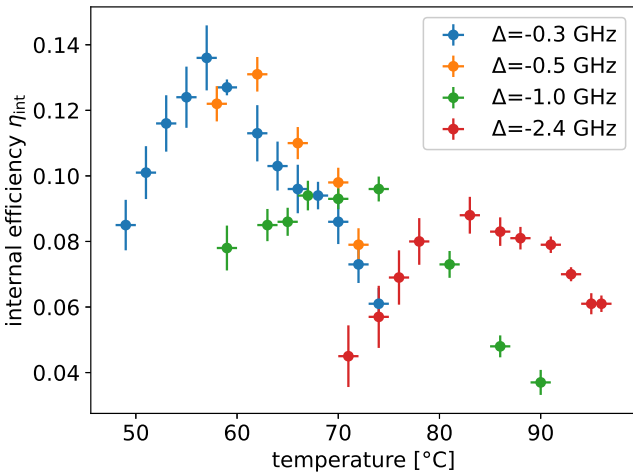


FIG. 4. Temperature dependence of the optimal working point of the memory. The OD is increased by raising the temperature of the cell. The larger the signal detuning Δ , the more OD is required to achieve the highest efficiency. For large detunings $\Delta < -1000$ MHz, the efficiency is limited by the available control power.

to quantify the spectral region in which photons of a given bandwidth can be stored efficiently. To estimate this spectral acceptance window of the memory \mathcal{AW} , we measure the internal efficiency over a scan of the two-photon detuning δ for a set of signal detunings, $\Delta = \{0, -300, -500, -1000\}$ MHz. This data set represents quantum light sources emitting photons in a spectral window around the target frequency. Studying the frequency-dependent internal efficiency enables estimation of upper limits to the frequency bandwidth and drift of the single-photon source to be interfaced. Taking the Fourier-limited linewidth of the signal laser, $\gamma_{\text{hom}} \approx 440$ MHz, into account, we can infer the spectral acceptance window of the memory from the data presented in Fig. 5. We use this result to estimate the influence of inhomogeneously broadened signals on the memory efficiency and SNR in the next section.

C. Benchmarks for Storage of Single Photons

By virtue of the spectral acceptance window we can estimate benchmark properties for true single-photon input that are required for successful storage experiments. We assume that the signal input is $\Delta = -500$ MHz red-detuned from the signal transition and that the memory acceptance window has a FWHM of $\mathcal{AW} = 560(60)$ MHz. Further assuming that the input photons have a Gaussian temporal envelope of about 1 ns FWHM and experience no spectral shift on the time scale of the experiment, we can estimate the compatibility of the memory with single-photon sources. In Fig. 6 we show the expected SNRs for different source efficiencies and inhomogeneous

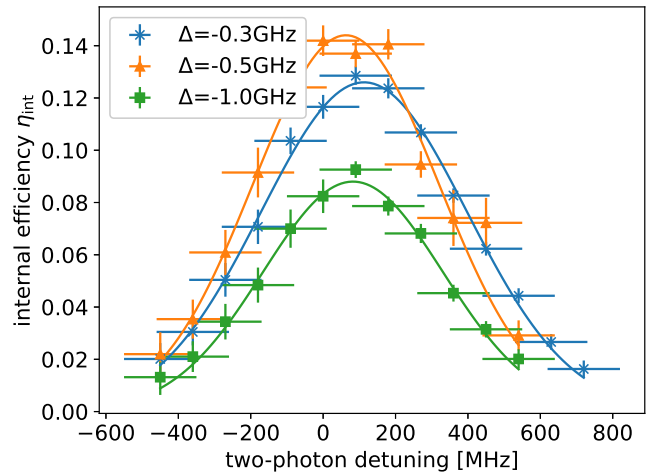


FIG. 5. Spectral acceptance window. Internal memory efficiency over two-photon detuning for different single-photon detunings and 1 ns signal pulse lengths. We scan the signal frequency keeping the control frequency fixed. The width of the curve corresponds to the spectral acceptance window of the memory convoluted with the input laser pulse. For $\Delta = -500$ MHz we extract $\mathcal{AW} = 560$ MHz.

linewidths γ_{inhom} of the input photons.

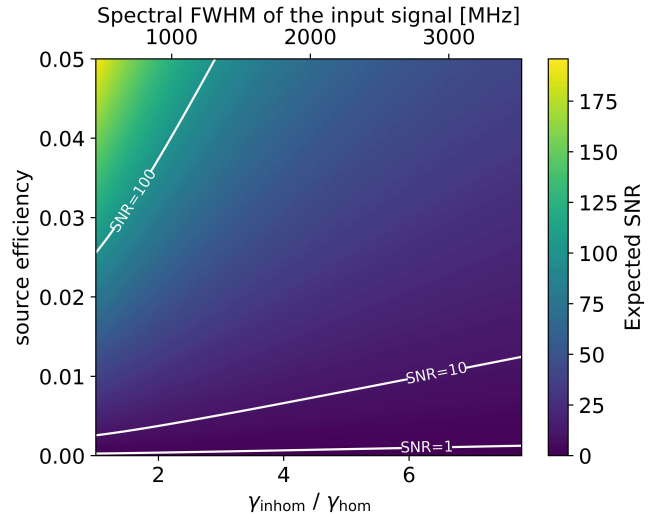


FIG. 6. Benchmarking the memory for single photons from a semiconductor quantum dot source with 500 MHz homogeneous linewidth. Influence of the photon extraction efficiency of the light source and the inhomogeneous linewidth γ_{inhom} of the emitted photons on the expected SNR of the storage signal.

The SNRs given in Fig. 6 form an upper bound as they rely on estimated internal memory efficiencies. The pulse generation with EOMs effectively limits the shape of the control pulses to Gaussians which will create a temporal mode mismatch between signal and control pulses. Considering the exponential shape of the QD single pho-

tons we expect the achievable efficiencies and SNRs to be lower. Additionally, the increased noise floor from unfiltered background emission will further lower the SNR in an experiment. In the case of quantum dot devices one can imagine undesired excitation of multiple emitters or collection of light from additional relaxation paths, e.g. bi-excitons, as noise sources.

V. DISCUSSION

We have demonstrated on-demand storage and retrieval of attenuated laser pulses with an average photon number of 0.06 in a room-temperature vapor ladder-type memory on the Cs D1 line. The memory achieves a maximum internal efficiency of $\eta_{\text{int}} = 15(1)\%$ and an end-to-end efficiency of $\eta_{\text{e2e}} = 2.2(2)\%$. The high SNR of 830(80) for ultra-weak signals and the broad spectral acceptance window of $\mathcal{AW} = 560(60)$ MHz promise compatibility of the memory with state-of-the-art solid-state single-photon emitters such as InGaAs quantum dots [36]. The variable control and signal pulse lengths, timings and pulse shapes in the experiment offer great flexibility when coupling the quantum dot single-photon source to the memory setup. Considering a typical InGaAs quantum dot sample [25], we expect single-photon emission with a pulse length of about 1 ns and a homogeneous linewidth of about 160 MHz which fits into the acceptance window of the memory. Even in the case of inhomogeneously broadened emission with a linewidth of about 2 GHz due to spectral diffusion we expect SNRs above 10.

VI. OUTLOOK

We see clear technological improvements that will increase the efficiency of the optical memory in future experiments. The implementation of optical hyperfine pumping will significantly boost the memory performance. The use of an anti-reflective coated cell will further increase the overall setup transmission and thereby the end-to-end efficiency. An active stabilization of the EOMs' DC-bias drifts will improve the pulse quality and the long-term stability of the experiment. To obtain a more homogeneous control field along the signal beam profile, we will aim at a larger difference in beam diameters in future experiments. The results show that the memory is compatible with state-of-the-art quantum light emitters. The interface of an external single-photon source with the memory poses a significant technological challenge, especially regarding wavelength matching, bandwidth, spectral drifts of the source, and synchronization. The aforementioned setup improvements will further facilitate the construction of a heterogeneous on-demand light-matter interface. The study of such systems may contribute to the development of optical quantum networks.

ACKNOWLEDGMENTS

We would like to thank Omri Davidson, Eilon Poem and Ofer Firstenberg for fruitful discussions. This work was funded by the DFG project RE2974/28-1 (448532670) and the German Ministry of Science and Education (BMBF) project Q-ToRX 16KISQ040K.

[1] A. I. Lvovsky, B. C. Sanders, and W. Tittel, *Nature Photonics* **3**, 706 (2009).

[2] K. Hammerer, A. S. Sørensen, and E. S. Polzik, *Rev. Mod. Phys.* **82**, 1041 (2010).

[3] K. Heshami, D. G. England, P. C. Humphreys, P. J. Bustard, V. M. Acosta, J. Nunn, and B. J. Sussman, *Journal of Modern Optics* **63**, 2005 (2016), <https://doi.org/10.1080/09500340.2016.1148212>.

[4] O. Davidson, O. Yogev, E. Poem, and O. Firstenberg, *Phys. Rev. Lett.* **131**, 033601 (2023).

[5] H.-J. Briegel, W. Dür, J. I. Cirac, and P. Zoller, *Phys. Rev. Lett.* **81**, 5932 (1998).

[6] X.-Y. Luo, Y. Yu, J.-L. Liu, M.-Y. Zheng, C.-Y. Wang, B. Wang, J. Li, X. Jiang, X.-P. Xie, Q. Zhang, X.-H. Bao, and J.-W. Pan, *Phys. Rev. Lett.* **129**, 050503 (2022).

[7] T. van Leent, M. Bock, F. Fertig, R. Garthoff, S. Eppelt, Y. Zhou, P. Malik, M. Seubert, T. Bauer, W. Rosenfeld, W. Zhang, C. Becher, and H. Weinfurter, *Nature* **607**, 69 (2022).

[8] Y. Lei, F. K. Asadi, T. Zhong, A. Kuzmich, C. Simon, and M. Hosseini, *Optica* **10**, 1511 (2023).

[9] Y.-A. Chen, Q. Zhang, T.-Y. Chen, W.-Q. Cai, S.-K. Liao, J. Zhang, K. Chen, J. Yin, J.-G. Ren, Z. Chen, S.-L. Han, Q. Yu, K. Liang, F. Zhou, X. Yuan, M.-S. Zhao, T.-Y. Wang, X. Jiang, L. Zhang, W.-Y. Liu, Y. Li, Q. Shen, Y. Cao, C.-Y. Lu, R. Shu, J.-Y. Wang, L. Li, N.-L. Liu, F. Xu, X.-B. Wang, C.-Z. Peng, and J.-W. Pan, *Nature* **589**, 214 (2021).

[10] J. Wallnöfer, F. Hahn, M. Gündoğan, J. S. Sidhu, F. Wiesner, N. Walk, J. Eisert, and J. Wolters, *Communications Physics* **5**, 169 (2022).

[11] M. Gündoğan, J. S. Sidhu, V. Henderson, L. Mazzarella, J. Wolters, D. K. L. Oi, and M. Krutzik, *npj Quantum Information* **7**, 128 (2021).

[12] K. F. Reim, J. Nunn, V. O. Lorenz, B. J. Sussman, K. C. Lee, N. K. Langford, D. Jaksch, and I. A. Walmsley, *Nature Photonics* **4**, 218 (2010).

[13] S. E. Thomas, T. M. Hird, J. H. D. Munns, B. Brecht, D. J. Saunders, J. Nunn, I. A. Walmsley, and P. M. Ledington, *Phys. Rev. A* **100**, 033801 (2019).

[14] E. Saglamyurek, A. Rastogi, K. Heshami, and L. J. LeBlanc, *Nature Photonics* **12**, 774 (2018).

[15] D. Main, T. M. Hird, S. Gao, E. Oguz, D. J. Saunders, I. A. Walmsley, and P. M. Ledingham, *Phys. Rev. A* **103**, 043105 (2021).

[16] K. T. Kaczmarek, P. M. Ledingham, B. Brecht, S. E. Thomas, G. S. Thekkadath, O. Lazo-Arjona, J. H. D. Munns, E. Poem, A. Feizpour, D. J. Saunders, J. Nunn, and I. A. Walmsley, *Phys. Rev. A* **97**, 042316 (2018).

[17] R. Finkelstein, E. Poem, O. Michel, O. Lahad, and O. Firstenberg, *Science Advances* **4**, eaap8598 (2018).

[18] S. Thomas, S. Sagona-Stopfel, Z. Schofield, I. Walmsley, and P. Ledingham, *Phys. Rev. Appl.* **19**, L031005 (2023).

[19] J. Wolters, G. Buser, A. Horsley, L. Béguin, A. Jöckel, J.-P. Jahn, R. J. Warburton, and P. Treutlein, *Phys. Rev. Lett.* **119**, 060502 (2017).

[20] G. Buser, R. Mottola, B. Cotting, J. Wolters, and P. Treutlein, *PRX Quantum* **3**, 020349 (2022).

[21] M. Gschrey, A. Thoma, P. Schnauber, M. Seifried, R. Schmidt, B. Wohlfeil, L. Krüger, J.-H. Schulze, T. Heindel, S. Burger, F. Schmidt, A. Strittmatter, S. Rodt, and S. Reitzenstein, *Nature Communications* **6**, 7662 (2015).

[22] Tobias Heindel, Je-Hyung Kim, Niels Gregersen, Armando Rastelli, and Stephan Reitzenstein, *Adv. Opt. Photon.* **15**, 613 (2023).

[23] R. Uppu, L. Midolo, X. Zhou, J. Carolan, and P. Lodahl, *Nature Nanotechnology* **16**, 1308 (2021).

[24] J. S. Wildmann, R. Trotta, J. Martín-Sánchez, E. Zallo, M. O’Steen, O. G. Schmidt, and A. Rastelli, *Phys. Rev. B* **92**, 235306 (2015).

[25] L. Bremer, S. Fischbach, S.-I. Park, S. Rodt, J.-D. Song, T. Heindel, and S. Reitzenstein, *Advanced Quantum Technologies* **3**, 1900071 (2020).

[26] H. Vural, S. Seyfferle, I. Gerhardt, M. Jetter, S. L. Portalupi, and P. Michler, *Phys. Rev. B* **103**, 195304 (2021).

[27] T. Kroh, J. Wolters, A. Ahlrichs, A. W. Schell, A. Thoma, S. Reitzenstein, J. S. Wildmann, E. Zallo, R. Trotta, A. Rastelli, O. G. Schmidt, and O. Benson, *Scientific Reports* **9**, 13728 (2019).

[28] G.-D. Cui, L. Schweickert, K. D. Jöns, M. Namazi, T. Lettner, K. D. Zeuner, L. Scavuzzo Montaña, S. Filipe Covre da Silva, M. Reindl, H. Huang, R. Trotta, A. Rastelli, V. Zwiller, and E. Figueroa, *arXiv e-prints*, arXiv:2301.10326 (2023), arXiv:2301.10326 [quant-ph].

[29] R. Al Maruf, S. Venuturumilli, D. Bharadwaj, P. Anderson, J. Qiu, Y. Yuan, M. Zeeshan, B. Semnani, P. J. Poole, D. Dalacu, K. Resch, M. E. Reimer, and M. Bajcsy, *arXiv e-prints*, arXiv:2309.06734 (2023), arXiv:2309.06734 [quant-ph].

[30] S. E. Thomas, L. Wagner, R. Joos, R. Sittig, C. Nawrath, P. Burdekin, T. Huber-Loyola, S. Sagona-Stopfel, S. Höfling, M. Jetter, P. Michler, I. A. Walmsley, S. L. Portalupi, and P. M. Ledingham, *arXiv e-prints*, arXiv:2303.04166 (2023), arXiv:2303.04166 [quant-ph].

[31] R. Finkelstein, O. Lahad, I. Cohen, O. Davidson, S. Kiriati, E. Poem, and O. Firstenberg, *Phys. Rev. X* **11**, 011008 (2021).

[32] A. V. Gorshkov, A. André, M. D. Lukin, and A. S. Sørensen, *Phys. Rev. A* **76**, 033806 (2007).

[33] M. Dujić, D. Buhin, N. Šantić, D. Aumiler, and T. Ban, Comparative study of light storage in antirelaxation-coated and buffer-gas-filled alkali vapor cells (2023), arXiv:2310.03726 [quant-ph].

[34] N. B. Phillips, A. V. Gorshkov, and I. Novikova, *Phys. Rev. A* **78**, 023801 (2008).

[35] A. Thoma, P. Schnauber, M. Gschrey, M. Seifried, J. Wolters, J.-H. Schulze, A. Strittmatter, S. Rodt, A. Carmele, A. Knorr, T. Heindel, and S. Reitzenstein, *Phys. Rev. Lett.* **116**, 033601 (2016).

[36] N. Tomm, A. Javadi, N. O. Antoniadis, D. Najer, M. C. Löbl, A. R. Korsch, R. Schott, S. R. Valentin, A. D. Wieck, A. Ludwig, and R. J. Warburton, *Nature Nanotechnology* **16**, 399 (2021).